

---

# DETECTING STATE CHANGES IN FUNCTIONAL NEURONAL CONNECTIVITY USING FACTORIAL SWITCHING LINEAR DYNAMICAL SYSTEMS

---

**Yiwei Gong**

Department of Statistics and Data sciences  
The University of Texas at Austin  
yiwei.gong@utexas.edu

**Susanna B. Mierau**

Department of Neurology  
Brigham and Women's Hospital and Harvard Medical School  
smierau@bwh.harvard.edu

**Sinead A. Williamson**

Apple Machine Learning Research  
sa\_williamson@apple.com

## ABSTRACT

A key question in brain sciences is how to identify time-evolving functional connectivity, such as that obtained from recordings of neuronal activity over time. We wish to explain the observed phenomena in terms of latent states which, in the case of neuronal activity, might correspond to subnetworks of neurons within a brain or organoid. Many existing approaches assume that only one latent state can be active at a time, in contrast to our domain knowledge. We propose a switching dynamical system based on the factorial hidden Markov model. Unlike existing approaches, our model acknowledges that neuronal activity can be caused by multiple subnetworks, which may be activated either jointly or independently. A change in one part of the network does not mean that the entire connectivity pattern will change. We pair our model with scalable variational inference algorithm, using a concrete relaxation of the underlying factorial hidden Markov model, to effectively infer the latent states and model parameters. We show that our algorithm can recover ground-truth structure and yield insights about the maturation of neuronal activity in microelectrode array recordings from in vitro neuronal cultures.

**Keywords** State space model · Factorial hidden Markov model · Auto-Encoding Variational Bayes · Neuroscience

## 1 Introduction

The brain receives information from the surrounding world before reacting correspondingly and systematically. As a complex system, it acts differently across time and locations. Thus, analytical tools that can detect correlations in spatial and temporal activity are required to study the brain's activity. The dynamic networks that underlie these brain processes at the microscale can be studied using microelectrode array (MEA) recordings of neural signals across a whole population of neural cells [27]. While MEA recordings do not allow us to target specific neurons, neural signals, highly correlated in time, from neurons near multiple electrodes can reveal the spatial-temporal features of

## Detect State Changes in Dynamic Networks

brain network function. Understanding this functional connectivity *in vitro* is important for understanding microscale brain function and development *in vivo* [10].

Previous studies of microscale functional neuronal networks have focused on the network topology [5, 26, 28]. These studies estimate a functional graph by considering pair-wise correlations between electrodes over a period of time. Graph theoretical metrics are then used to compare the topology of the functional networks including the spatial arrangement of nodes [27]. These approaches have two important limitations. Firstly, they estimate a single pattern of functional connectivity based on minutes of MEA recording. This ignores the fact that brain networks are adaptable on much faster time-scales and precludes study of such short-term changes in connectivity. Secondly, they rely on pair-wise comparison of nodal activity to determine functional connectivity, which may not capture patterns of activity observed in subnetworks detected by more than two electrodes.

Other works have used discrete state-space models to capture evolving functional connectivity. These approaches capture the idea that a dynamical system—in our case, temporal MEA recordings—can be explained in terms of a small number of underlying behavioral patterns. In the simplest state-space model, hidden Markov models (HMMs) model neuronal activity as arising from one of a small number of underlying activity patterns [24]. Switching linear dynamical systems (SLDS) extend this by characterizing each activity pattern using a linear dynamical system [25]. Extensions add additional structure between the latent states, allowing for more flexible dynamics [16, 20, 6]. These approaches, however, make the unrealistic assumption that neuronal activity can be partitioned into a small number of *a priori* independent activity patterns. They lack the capacity to detect multiple network patterns simultaneously, as occurs in complex brain networks.

New methods are needed to identify changes in functional connectivity across seconds to minutes during MEA recordings, without making unrealistic assumptions about the nature of connectivity changes. In this work, we posit that neuronal activity can be decomposed into multiple subnetworks that can be activated jointly or separately. This allows us to capture overlapping patterns of behavior without the need to create a single state for each combination of active subnetworks. Factorial Switching Linear Dynamical Systems (FSLDS) replaces the single discrete latent state model at the heart of SLDS-based models with a factorial latent state model [FHMM, 8], modeling MEA recordings in terms of latent features (or subnetworks) that can be turned on or off independently. Active subnetworks evolve according to a linear dynamical system. To facilitate inference, we formulate our latent state model using a continuous relaxation of the factorial hidden Markov model [18] and perform inference using autoencoded variational Bayes [AEVB, 12]. We first explore properties of FSLDS on simulated data, validating its ability to recover ground-truth additive latent structure. Second, we show how it can uncover interpretable latent structure in MEA recordings. Third, we show how it reveals a developmental increase in the number of latent features (or subnetworks) in human induced pluripotent stem cell (iPSC)-derived neuronal networks *in vitro*.

## 2 Background

Our model is a factorial state-space model that extends existing time-series models by allowing multiple latent factors to be active at once, using a continuous relaxation of a factorial hidden Markov model [FHMM, 8] to control which combination of latent factors are active. This leads to a more interpretable model for temporally evolving neuronal functional connectivity, where we assume that observations are generated from an additive combination of multiple subnetworks, that may not all activate synchronously. In this section, we review existing work in state space models for time series data, with a particular focus on models appropriate for modeling MEA recordings, and discuss inference approaches appropriate for complex discrete state-space models. We then review the FHMM in Section 2.3, which will form the backbone of our approach.

### 2.1 Modeling functional connectivity using discrete state space models

Discrete state-space models such as hidden Markov models [HMMs, 7] provide an interpretable model for time-series data, where we assume that each time-point belongs to one of a finite number of states. Observations are assumed iid given a state-specific emission-distribution. HMMs have been used to uncover latent structure in neuronal activity [3, 32, 15]. Switching dynamical systems replace the emission model with a dynamical system. The simplest example of this is a switching linear dynamical system [SLDS, 1], where a Markovian discrete state process switches between autoregressive models with state-specific parameters, which can lead to a more flexible model for MEA recordings [25]. Building on SLDS, more sophisticated models have been developed to handle more complex scenarios, such as recurrent switching linear dynamical system [rSLDS, 16] and tree-structured rSLDS [20]. These models introduce recurrent dependency structures, allowing memory between consecutive time points. Additionally, when linear assumptions prove insufficient, nonlinear dynamical system methods have been proposed [4, 29]. [21] introduces a variational RNN model with attention to incorporate both nonlinear dynamics and non-Markovian switches.

### 2.2 Bayesian inference for discrete state space models

The posterior distributions over the parameters of discrete state space models are often learned through Markov chain Monte Carlo (MCMC) using forward filtering backward sampling [31, 9, 22]. However, as model complexity increases, MCMC methods can suffer from slow mixing and high computational cost. Recent advances in variational inference provide a more computationally efficient alternative.

Auto-Encoding Variational Bayes (AEVB) [12] offers a flexible “black box” variational inference framework by using neural networks to specify a variational approximation and using gradient descent to optimize a sample-based estimate of the ELBO. However, gradient-based optimization methods cannot directly learn discrete variables, such as those present in switching dynamical systems. The REINFORCE algorithm [30] uses a Monte Carlo estimate of the gradient; however this estimate suffers from high variance [23]. Other approaches combine variational inference with sequential Monte Carlo [17, 19, 14, 13].

An alternative approach is to sidestep the use of discrete distributions altogether. The Concrete, or Gumbel-Softmax, distribution [11, 18],

$$p_{\alpha, \phi}(x) = (K - 1)! \phi^{K-1} \prod_{k=1}^K \left( \frac{\alpha_k x_k^{-\phi-1}}{\sum_{j=1}^K \alpha_j x_j^{-\phi}} \right) \tag{1}$$

is a continuous distribution over the probability simplex that can be used as an approximation to a Categorical( $\alpha_1, \dots, \alpha_K$ ) distribution. The temperature parameter  $\phi$  controls the smoothness of the distribution; by annealing the temperature  $\phi$ , the posterior distribution of the continuous approximation asymptotically converges to the discrete Categorical distribution as  $\phi \rightarrow 0$ . Since the Concrete( $\alpha, \phi$ ) distribution is continuous, we can use it directly in variational inference as an alternative to the Categorical distribution.

### 2.3 Factorial Hidden Markov Models

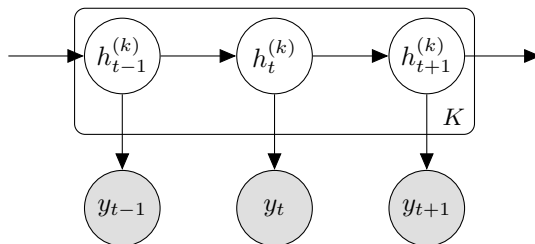


Figure 1: Graphical model for a factorial hidden Markov models.  $K$  discrete Markovian processes jointly influence the observation  $y_t$ . By contrast, a standard hidden Markov model is controlled by a single discrete process.

## Detect State Changes in Dynamic Networks

HMMs (and the more complex switching dynamical systems described in Section 2.1) assume that, at any given time point, observations are generated according to a single latent emission model. This may be unrealistic in complex time series such as MEA recordings.

In practice, two timepoints may share some characteristics, but not others. This observation motivates the factorial hidden Markov model [FHMM, 8], where multiple hidden factors  $\{h_t^{(k)}\}_{k=1}^K$  concurrently influence the observed dynamics at each time point  $y_t$ .

$$\begin{aligned} h_t^{(k)} | h_{t-1}^{(k)} &\sim \text{Categorical} \left( \pi_{h_{t-1}^{(k)}}^{(k)} \right) \\ y_t | h_t^{(1)}, \dots, h_t^{(K)} &\sim f \left( \theta_{h_t^{(1)}}, \dots, \theta_{h_t^{(K)}} \right). \end{aligned} \quad (2)$$

Each latent factor  $h_t^{(k)}$  evolves according to an independent Markovian process with transition probabilities  $\pi^{(k)}$ . The emission process at time  $t$  depends on the states of all  $K$  latent factors, as depicted in Figure 1. Typically,  $f(\cdot)$  is an additive model that combines state-specific features  $\theta_{h_t^{(k)}}$ .

### 3 A factorial switching linear dynamical system for modeling functional connectivity from MEA recordings

We propose factorial switching linear dynamical systems (FSLDS), a factorially switching linear dynamical model appropriate for capturing functional connectivity patterns. We begin, in Section 3.1, by introducing a continuous relaxation of the FHMM, which serves as the backbone of our approach, which we present in Section 3.2. Replacing the discrete FHMM with a continuous relaxation allows us to perform variational inference without the need to explicitly enumerate over combinations of latent factors, as we describe in Section 3.3.

#### 3.1 ConcreteFHMM

The factorial nature of the FHMM leads to an exponentially growing parameter space. Exploration of this discrete state space is challenging, and traditional MCMC methods are prone to difficult and slow mixing [8]. As we discussed in Section 2.2, variational inference provides an appealing alternative to MCMC, allowing us to exploit optimization techniques to learn an approximate posterior. However, as we saw, a naive implementation of variational inference methods does not allow for discrete latent states, since gradient descent is inherently designed for continuous variables.

To overcome this limitation, we introduce a continuous variant of the FHMM by relaxing the discrete latent state indicators into continuous variables using the Concrete distribution (Equation 1). We assume  $h_t^{(k)} \in [0, 1]$  and an additive emission model  $f_\theta$ , so that  $h_t^{(k)}$  can be seen as turning on or off the  $k$ th latent feature.

$$\begin{aligned} h_t^{(k)} | h_{t-1}^{(k)} &= \text{Concrete} \left( f_p \left( h_{t-1}^{(k)}, y_{t-1} \right), \phi \right) \\ y_t | h_t^{(1)}, \dots, h_t^{(K)} &\sim f_y \left( \sum_{k=1}^K \theta_k h_t^{(k)} \right). \end{aligned} \quad (3)$$

The binary discrete Markovian processes in Equation 2 are replaced by continuous indicators of the degree of contribution of the  $k$ th latent factor  $\theta_k$ . This provides significant computational benefits, as it enables the use of gradient-based optimization techniques that are more scalable and efficient than sampling-based methods.

In a FHMM, each latent factor is associated with a transition matrix that describes the probability of transitioning between states. In the ConcreteFHMM, we no longer have discrete state indicators (as  $h_t^{(k)}$  is continuous). Since we cannot use these continuous indicators to directly index a row of the transition matrix, we introduce a function  $f_p$  to specify the distribution over the value of the  $k$ th latent factor at time  $t$ . In our experiments, we parametrize  $f_p$  using a recurrent neural network.

## Detect State Changes in Dynamic Networks

The computational advantage of using a continuous relaxation comes with the trade-off of losing directly interpretable transition probabilities that are inherent in discrete Markov processes. However, setting an appropriately low temperature means that in practice, we tend to have values that are very close to zero or one, as we see in Section 4. As we will see, this allows us to retain some level of interpretability, bridging the gap between computational efficiency and the practical understanding of the model’s behaviour.

### 3.2 Factorial switching linear dynamical systems

As we have seen, HMMs, SLDSs, and their variants assume each time point corresponds to a single latent state. In practice, this might be unrealistic. For example, in developing brains, we expect new subnetworks to appear in addition to previous structure, rather than fully replacing the previous connectivity pattern. Further, we do not expect a subnetwork to have constant activity—instead, we want to disentangle changes in activity amplitude from changes in neuron connectivity. To achieve this, we separate these processes by first determining whether a feature is active using a ConcreteFHMM, and then modeling the value of the state when it is active using a linear dynamical system. The generative model is

$$\begin{aligned}
 y_{t,m} &\sim \text{Poisson} \left( \sum_{k=0}^K \theta_{k,m} h_t^{(k)} \exp \{ z_t^{(k)} \} \right), & m = 1, \dots, M \\
 h_t^{(0)} &= 1, \\
 h_t^{(k)} \mid h_{t-1}^{(k)} &\sim \text{Concrete} \left( f_p \left( h_{t-1}^{(k)}, y_{t-1} \right) \right), & k = 1, \dots, K \\
 z_t^{(k)} \mid z_{t-1}^{(k)} &\sim \text{Normal} \left( A z_{t-1}^{(k)}, \sigma_p^2 \mathbb{I} \right), & k = 0, \dots, K.
 \end{aligned} \tag{4}$$

The level of activity of the  $k$ th subnetwork is governed by two components: an (approximately) discrete state  $h_t^{(k)}$ , and a continuous state  $z_t^{(k)}$ . The approximately discrete state  $h_t^{(k)}$  controls whether a subnetwork is currently contributing to the rate, and aids in interpretability of the latent structure. Meanwhile the continuous states  $z_t^{(k)}$  control variation in the amplitude of the activity. In the context of MEA recordings, we can think of  $h_t^{(k)}$  as indicating whether a subnetwork is currently active, and  $\exp \{ z_t^{(k)} \}$  as controlling variation in its activity while it is active. We summarize FSLDS in Figure 2.

The latent feature indicators  $h_t^{(k)}$  follow a ConcreteHMM, as described in Section 3.1. The choice of a ConcreteFHMM is primarily due to computational practicality; as we will see in Section 3.3, this allows us to easily optimize a variational approximation to the posterior. In addition, it allows for a more complex recurrent dependency on the observed data, via the neural network  $f_p$ , instantiated using a recurrent neural network. The continuous latent variables  $z_t^{(k)}$  follow an autoregressive model, parametrized by a time-invariant matrix  $A$  and a diagonal noise term  $\sigma_p^2$ .

At each time  $t$ , each entry of the  $M$ -dimensional observation  $y_t$  is sampled according to a Poisson distribution parameterized by additive rates.<sup>1</sup> The  $K$  components in the additive rates can be seen as activities from  $K$  subnetworks or motifs, the structure of which is given by  $\theta_k$ . In our MEA application, we can think of  $\theta_k$  as specifying the relative contributions of each electrode to a subnetwork.

### 3.3 Inferring latent states using variational inference

In order to effectively learn the latent states  $\Theta = \{h_t, z_t\}_{t=1}^T$  we develop an AEVB algorithm inspired by [2]. Our algorithm makes use of a variational distribution  $q(\Theta) = \prod_t q(h_t)q(z_t)$  to approximate the posterior of the model defined in Equation 4. We parametrize  $q(\Theta)$  using a combination of neural networks,

<sup>1</sup>We use a Poisson distribution since our application uses spike count data, but alternative choices could be used here.

## Detect State Changes in Dynamic Networks

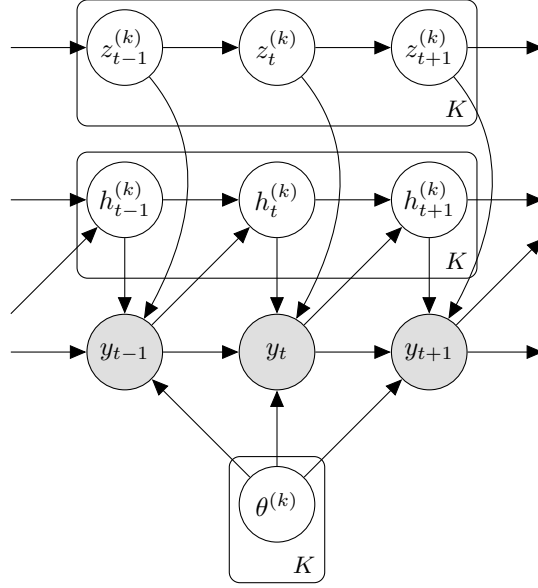


Figure 2: FSLDS: a factorial switching linear dynamical system for decomposing functional connectivity patterns.

$$\begin{aligned} q(h_t^{(k)}) &= \text{Concrete} \left( f_q \left( h_{t-1}^{(k)}, y_t \right) \right) \\ q(z_t^{(k)}) &= \text{Normal} \left( f_z \left( z_{t-1}^{(k)}, y_t \right), \sigma_q^2 \right). \end{aligned} \quad (5)$$

Here, our variational distribution  $q(h_t^{(k)})$  for the discrete latent states is parametrized by an RNN  $f_q$ , and the variational distribution  $q(z_t^{(k)})$  for the continuous latent states is parameterized by an RNN  $f_z$ . Each RNN depends both on the previous states and on the current observation.

We then optimize the ELBO, following [12]. We treat  $\sigma_p$ ,  $\sigma_q$ , and  $A$  as parameters to be optimized using stochastic gradient descent. To encourage sparsity in the inferred latent structure, we add an L1 penalty  $\lambda \sum_t \sum_k h_t^{(k)}$  on the learned  $h_t^{(k)}$  to the ELBO.

## 4 Experimental evaluation

In this section, we evaluate FSLDS on a series of real and synthetic datasets. For all experiments, we represent  $f_q$ ,  $f_p$  and  $f_z$  using recurrent neural networks with 64 hidden dimensions. The temperature for the Concrete distribution was gradually annealed from 1 at a rate of 0.00003 until it reached a final value of 0.1. In the simulated data experiments, we set a learning rate of 0.01 for all parameters except for  $\theta$ , which initially had a learning rate of 0.1 that was reduced to 0.01 after the first 200 epochs. For real data experiments, we used a learning rate of 0.001 for all parameters, again with  $\theta$  starting at 0.1 and decreasing to 0.001 after 200 epochs. We augment the ELBO with an L1 penalization term  $\lambda \sum_t \sum_k h_t^{(k)}$ , with  $\lambda = 0.2$ ; this value was found to give good performance on synthetic data. For each value of  $K$ , we use 75 different random initializations and select the run with the lowest ELBO.

In our model, since  $\theta_k$  is always multiplied by  $e^{z_t^{(k)}}$ , the scales of  $\theta_k$  and  $z_t^{(k)}$  are non-identifiable. In our visualizations, we rescale the inferred  $\theta_k$  so that its maximum value is one and adjust the values of  $z_t^{(k)}$  accordingly. For the real data, the spike counts exhibit a very heavy tailed distribution. For this reason, when visualizing the raw data and the continuous activities  $e^{z_t^{(k)}}$ , we truncate our visualization at the 95th percentile of the raw spike count values. When visualizing the latent subgraphs  $\theta_k$ , we only show subgraphs appearing in at least 5% of time points.

## Detect State Changes in Dynamic Networks

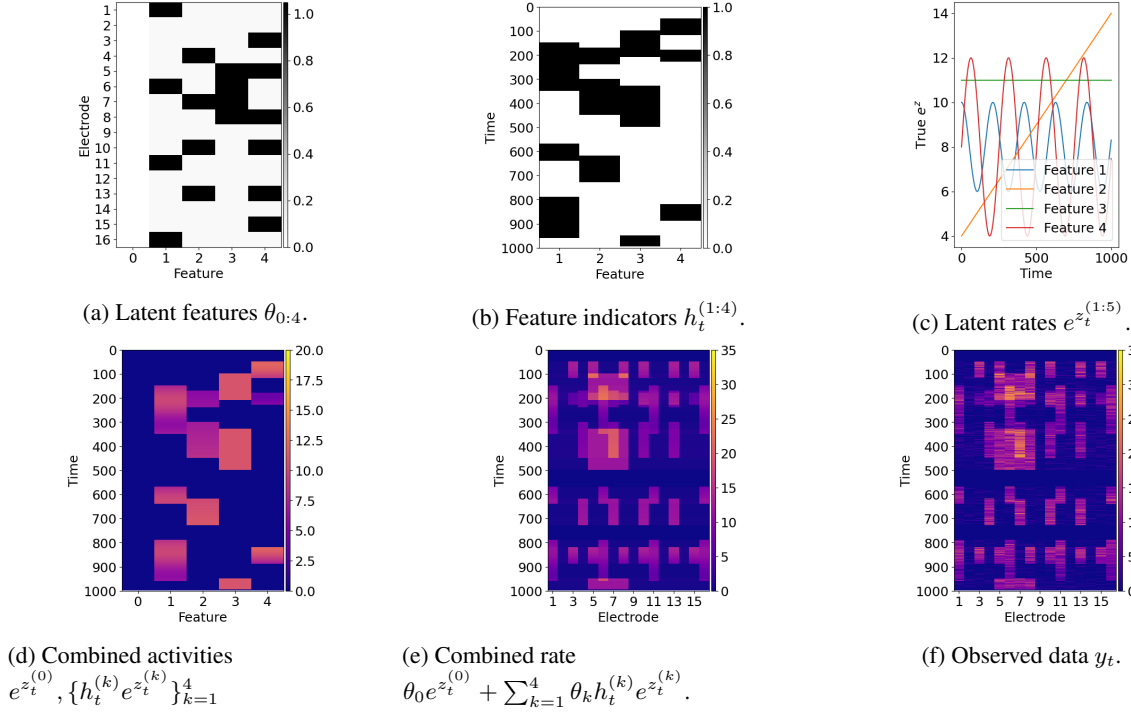


Figure 3: Synthetic data: Ground truth.

### 4.1 Simulated Data

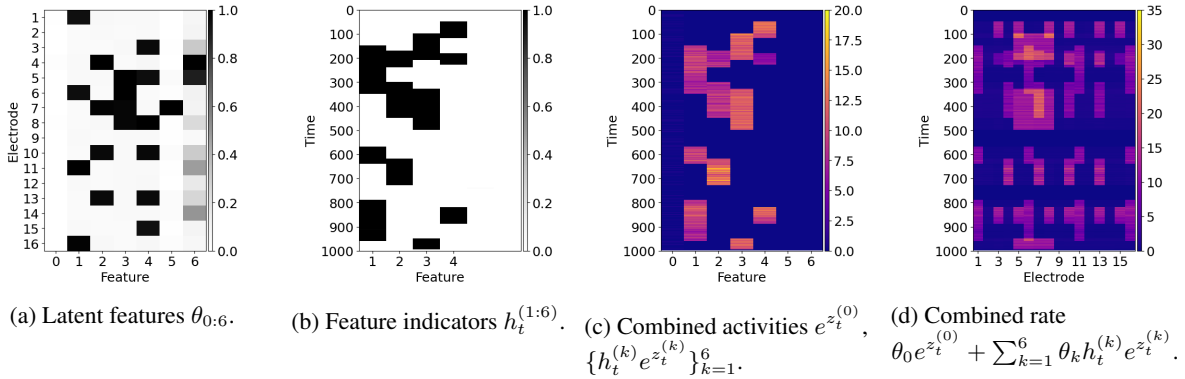


Figure 4: Synthetic data: Posterior mean obtained using AEVB. Note that, since the inferred  $h_t^{(5)}$  and  $h_t^{(6)}$  are zero everywhere, features  $\theta_5$  and  $\theta_6$  in Figure 4a not contribute to the model.

We begin by exploring the performance of FSLDS in a synthetic example where the ground truth features are known (but not generated from the model). This allows us to explore the ability to recover latent structure and showcase the benefits of using a factorial model over a simpler SLDS. We generate  $T = 1000$  time steps, with  $K = 4$  latent, 16-dimensional features  $\theta_k$ , as shown in Figure 3a. Each figure has a latent continuous trajectory  $z_t^{(k)}$  drawn either from a straight line or a sinusoid, as shown in Figure 3c. These were combined with manually generated binary trajectories  $h_t^{(k)}$  (Figure 3b, Figure 3d) to obtain the rate shown in Figure 3e. This rate was used to sample random Poisson observations.

In Figure 4, we show the posterior means obtained via the inference procedure described in Section 3.3. The results indicate that the Poisson rates are accurately recovered and are appropriately decomposed into the true generating features, demonstrating the model's ability to capture the underlying structure of the data. Even though we set  $K = 6$ ,

## Detect State Changes in Dynamic Networks

the model correctly identifies the 4 latent features shown in Figure 3. We note that, while the ConcreteFHMM uses a continuous-valued indicator  $h_t^{(k)}$ , in practice the values obtained are very close to zero or one (Figure 4b); we see similar behavior in all other experiments in this section.

Next, we consider the latent structure we would find using a non-factorial method. In the left hand side of Figure 5, we have converted the thirteen combinations of latent features apparent in Figure 3b into thirteen distinct states. Already, we see this (true!) latent structure is less interpretable than the additive version in Figure 3b, since it requires over three times as many features to convey the same information. To attempt to learn this true, non-additive structure, we run

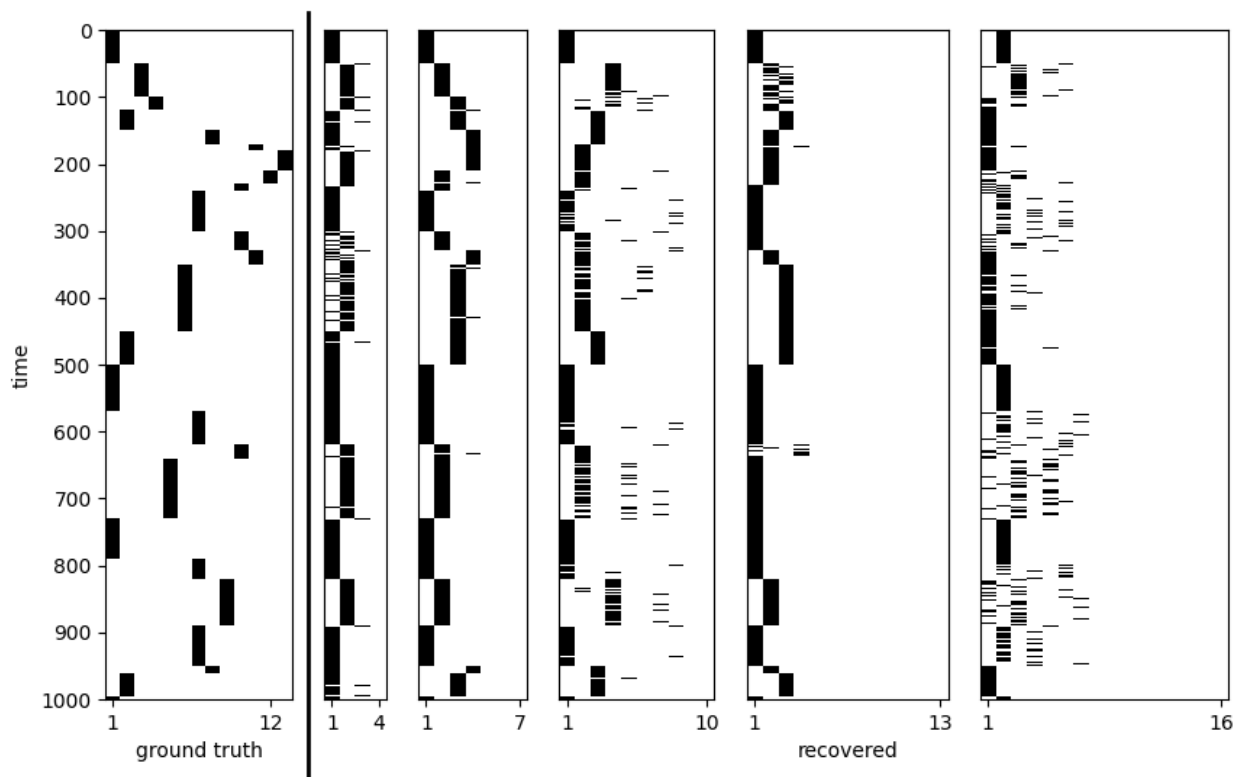


Figure 5: Latent states obtained using rSLDS. Left hand plot shows the ground truth latent states (corresponding to the twelve unique combinations of four additive features shown in Figure 3b). Remaining plots show the results with varying numbers of latent states, from four to sixteen.

recurrent SLDS (rSLDS), using the `ssm` package associated with the original paper [16]. We test rSLDS with  $K=4, 7, 10, 13$  and  $16$  features (with the correct number being  $13$ ), taking the best ELBO out of ten random seeds. The resulting state assignments shown in Figure 5. We see that we cannot recover the ground truth. We find that rSLDS tends to miss low-occupancy features and combine multiple features. Even though most of the plots show between two and four main features, these features are not consistent between plots. The results also tend to be noisier than those obtained using FSLDS, particularly as the number of features increases.

### 4.2 Evaluation of microelectrode array spike train data

To evaluate the performance of our algorithm on real-world neuronal connectivity data, we look at two datasets obtained via MEA recordings. For both datasets, we use preprocessed data from [28]. To obtain this data, spikes (action potentials) were detected from the raw MEA voltage time series, based on the action potential waveform using the continuous wavelet transform method implemented in MEA-NAP, a MATLAB pipeline for MEA network analysis[28].<sup>2</sup>

<sup>2</sup><https://github.com/SAND-Lab/MEA-NAP>



## Detect State Changes in Dynamic Networks

The voltage timeseries were acquired at a sampling rate of 12500 Hz (human iPSC-derived neuronal cultures) and 25000 Hz (murine hippocampal cultures). Action potentials are approximatedly 1ms in duration. For our analysis, we aggregated the spike train data to 1 second time bins.

### 4.2.1 Exploring properties of the inferred structure using murine hippocampal recordings

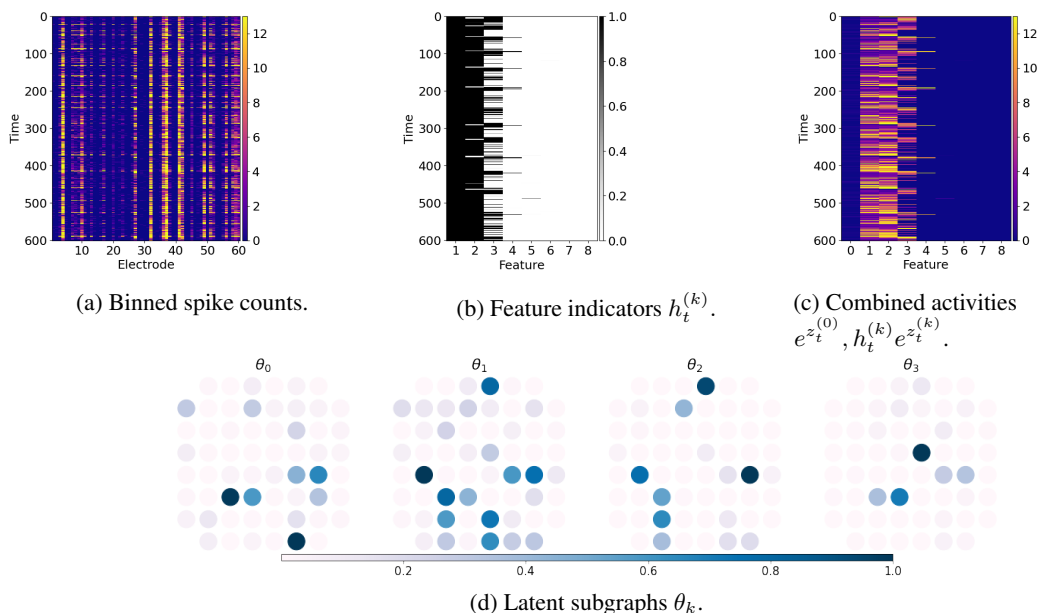


Figure 6: Murine hippocampal data (recording TC043 DIV14). Figure 6a shows the spike counts (color bar, truncated to the 95th percentile value) from a 10-minute MEA recording of a days-in-vitro (DIV) 14 primary hippocampal culture. The activity observed in each electrode (columns) is shown over time (y-axis unit is seconds). Spike count binned by 1 second intervals. Figure 6b shows the binary feature indicators  $h_t^{(k)}$ , indicating which of the latent features are active at each time point. Figure 6c shows the expression level of each of the latent features  $\theta_k$ . Figure 6d shows the relative contribution of each electrode, in the spatial arrangement of the MEA, for a subset of the latent states  $\theta_k$ , including the background (subnetwork 0) and most active subnetworks (1-4). The relative contribution (node color) is scaled for each subnetwork.

We first consider qualitative analyses based on MEA recordings from two 2D murine hippocampal cultures, first published in [26], using the spike train data from [28]. We visualize the neuronal activity from these two recordings in Figures 6a and 7a. The remaining subplots in Figures 6 and 7 show the latent structure obtained using FSLDS. In each case, we see the activity decomposed into distinct subgraphs (Figures 6d and 7d). Some features are active throughout most of the recording, but with varying levels of activity (e.g., features 1 and 2 in Figure 6). Others are active in short bursts, such as features 3 and 4 in Figure 6.

One concern might be that the number of inferred latent features will grow with sequence length regardless of the true latent dimensionality. To demonstrate this is not the case, in Figure 8, we concatenate the recording shown in Figure 6 with itself and re-run our analysis. We find there are still 4 main features, and the four features are almost the same as the features from using one single copy of the TC043 DIV14 recording (c.f. Figures 6d and 8d). Additionally, the activation patterns in the concatenated part is almost the same as the first half, indicating that the model does not create arbitrary patterns due to longer recordings.

In contrast, Figure 9 shows the same recording concatenated with a second recording (TC165 DIV14, as shown in Figure 7). Here, we would expect the structure for the first recording to be similar to that obtained in Figure 6, but unlike the previous example, we do not expect these features to persist into the second recording. Instead, we would expect to see latent structure similar to Figure 7. We see both halves of the concatenation use completely different

## Detect State Changes in Dynamic Networks

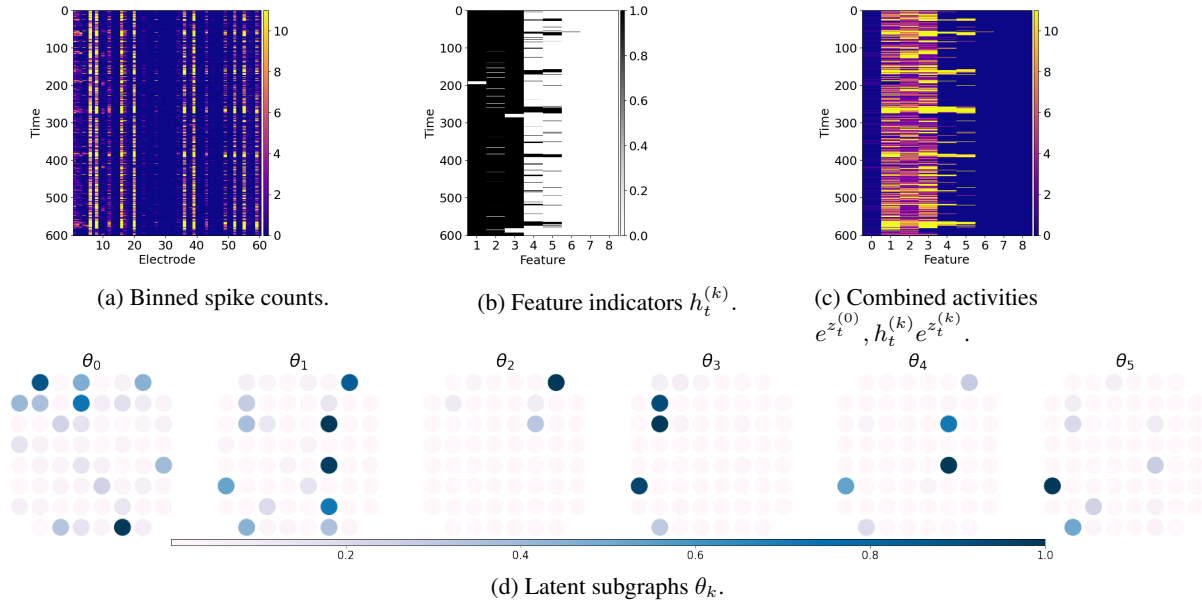


Figure 7: Murine hippocampal data (recording TC165 DIV14). Figure 7a shows the spike counts (color bar, truncated to the 95th percentile value) from a 10-minute MEA recording of a days-in-vitro (DIV) 14 primary hippocampal culture. The activity observed in each electrode (columns) is shown over time (y-axis unit is seconds). Spike count binned by 1 second intervals. Figure 7b shows the binary feature indicators  $h_t^{(k)}$ , indicating which of the latent features are active at each time point. Figure 7c shows the expression level of each of the latent features  $\theta_k$ . Figure 7d shows the relative contribution of each electrode, in the spatial arrangement of the MEA, for a subset of the latent states  $\theta_k$ , including the background (subnetwork 0) and most active subnetworks (1-4). The relative contribution (node color) is scaled for each subnetwork.

features—despite the fact that some electrodes, such as Electrode 36, appear relatively active in both Figures 6a and 7a. We also see that the activation features remain similar to the single recordings.

# Detect State Changes in Dynamic Networks

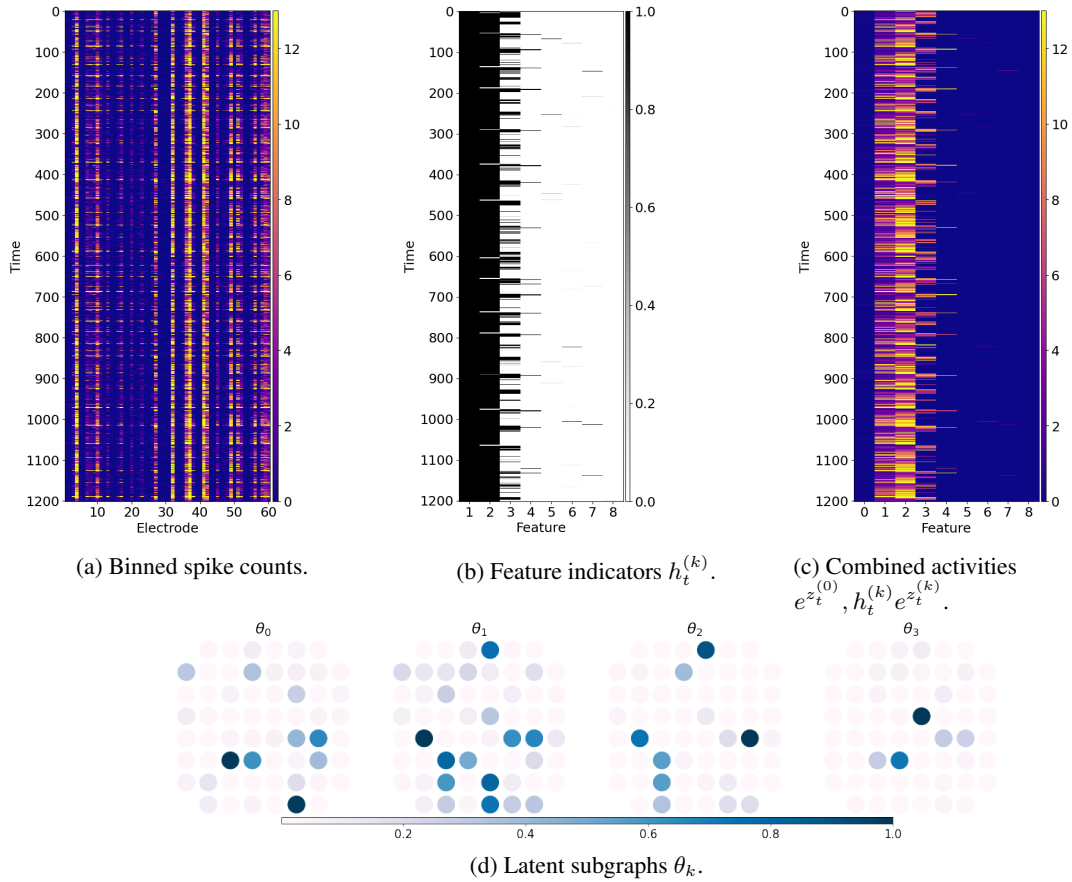


Figure 8: Murine hippocampal data (recording TC043 DIV14), duplicated, and concatenated, creating a 12-minute data series. Figure 8a shows the spike counts (truncated to the 95th percentile value) for the recording (1st copy 0-600 seconds, 2nd copy 600-1200 seconds). Figure 8b shows the binary feature indicators  $h_t^{(k)}$ , indicating which of the latent features are active at each time point. Figure 8c shows the expression level of each of the latent features  $\theta_k$ . Figure 8d shows the relative contribution of each electrode, in the spatial arrangement of the MEA, for a subset of the latent states  $\theta_k$ , including the background (subnetwork 0) and most active subnetworks (1-4).

# Detect State Changes in Dynamic Networks

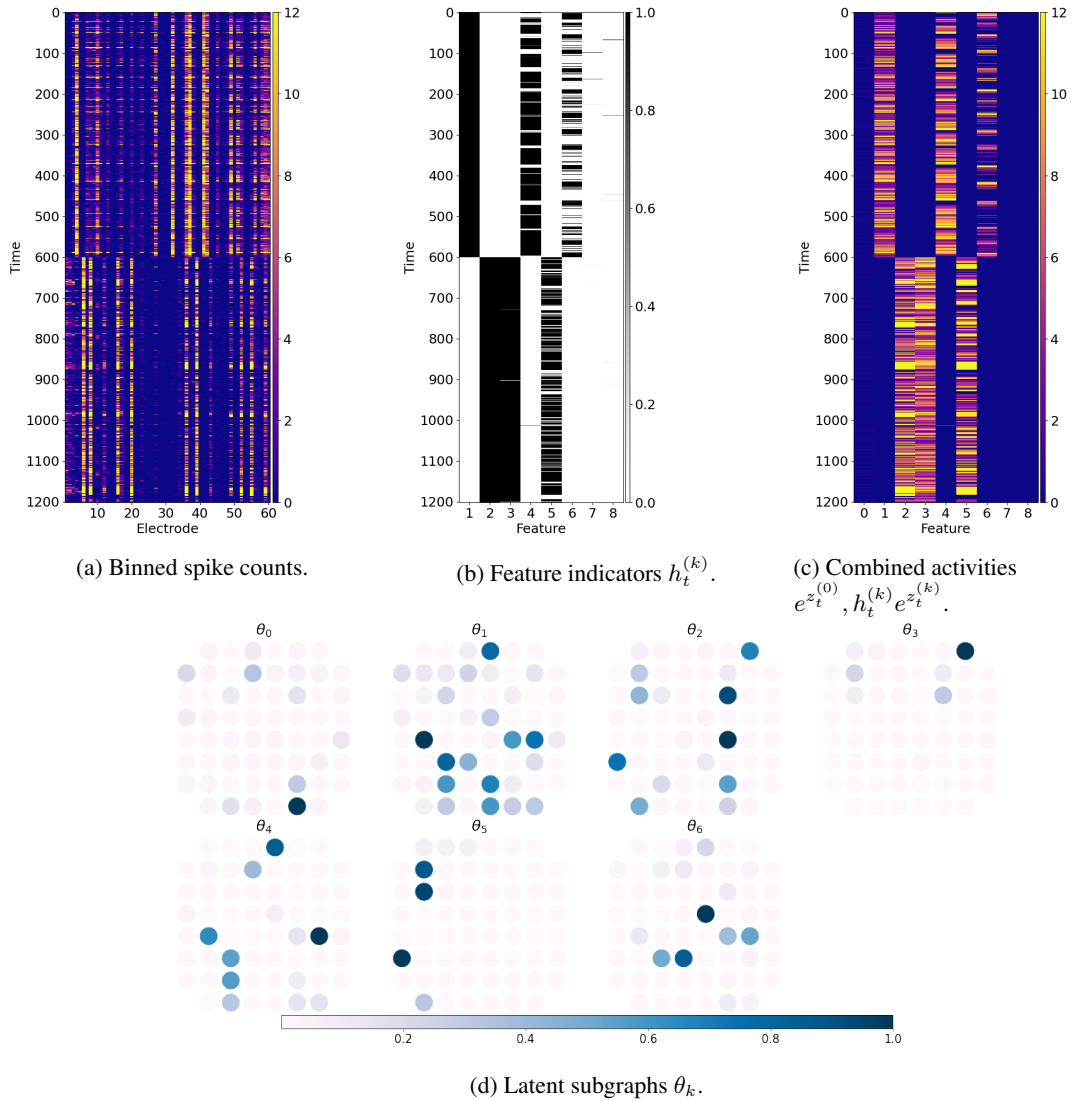


Figure 9: Murine hippocampal data (recordings TC043 DIV14 and TC165 DIV14) concatenated, creating a 12-minute time series. Figure 9a shows the spike counts (truncated to the 95th percentile value) for the two recordings (1st culture 0-600 seconds, 2nd culture 600-1200 seconds). Figures 9b–9c show inferred latent structure. Figure 9d shows subgraphs, in the spatial arrangement of the MEA, for the subnetworks (0-6).

### 4.2.2 Exploring evolution of connectivity over longer time periods

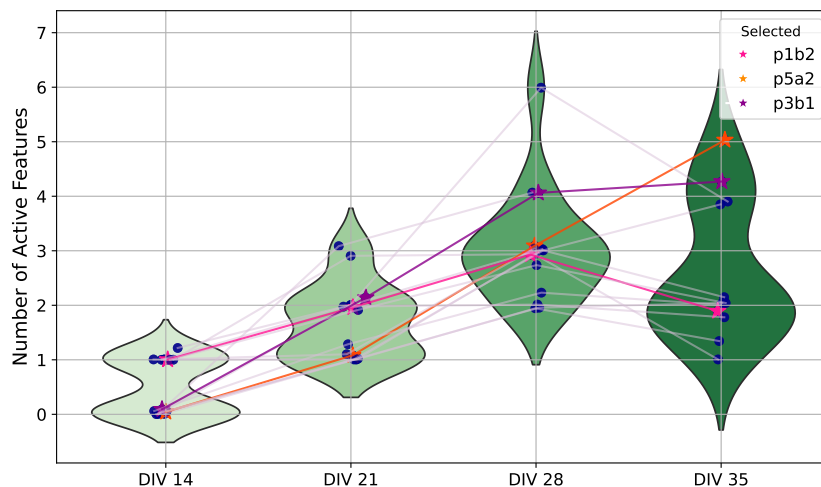


Figure 10: Number of activated features across weeks in culture. Violin plots with scatter plots of number of active features for each culture (circles or stars,  $n=15$  cultures) at four developmental time points days-in-vitro (DIV) 14, 21, 28, and 35. Lines show developmental trajectory of number of latent features within individual cultures. Three examples are highlighted with stars and thicker colored lines: P1B2 (pink, see also Figure 12), P5A2 (orange, see also Figure 13), and P3B1 (purple, see also Figure 14).

Next, we consider a dataset of MEA recordings from human induced pluripotent stem cell (iPSC)-derived neurogenin-2 (NGN2) cortical neurons cultured on 64-electrode MEAs ( $n=15$  cultures), first analyzed in [28]. Each culture was recorded for a period of ten minutes once per week, over a period of four weeks, at days-in-vitro (DIV) 14, 21, 28 and 35 for  $n = 15$  cortical cultures. Spike counts were binned into one-second intervals. To investigate subnetwork development in vitro, we concatenated the data from all four weeks for each culture.

We expect the level of functional connectivity to increase as the neuronal networks mature, reflected in both the number of active subnetworks and the overall complexity of the resulting network. We expect changes in the neuronal activity at the end of each recordings at the different days-in-vitro (since they correspond to temporal discontinuities) and changes in the latent structure within each time period. We set a maximum of 10 latent features and ran our variational algorithm using seventy-five different seeds, selecting the result with the highest ELBO.

In Figure 10, we show the average number of active features (or subnetworks) for each week, for each recording. In almost all cultures, we see an increase in the number of active features across the four weeks, suggesting a developmental process. This coincides with an increase in the number of active electrodes and the number of action potentials detected by these electrodes [28]. However, this pattern diverges at DIV 35, where a bimodal behaviour in the dataset is observed. While a few cultures continue to show a similar number (or increase) in the number of subgraphs at DIV 35 compared to DIV 28 (e.g., Figures 13), in other cultures, this number decreases (e.g., Figure 12). These likely represent more mature cultures in which the increase in the degree of connectivity has led to a consolidation of subgraphs between DIV 28-35 (see [28]).

In Figure 11, we look at the overlap between the connectivity across different weeks. We average  $h_t^{(k)}$  over each week and concatenate to get a  $K$ -dimensional vector. We then calculate the cosine similarities between these vectors. High values indicate high overlap between the average connectivity patterns; low values indicate little overlap. We see moderate overlap adjacent weeks, but low overlap over longer timescales.

## Detect State Changes in Dynamic Networks

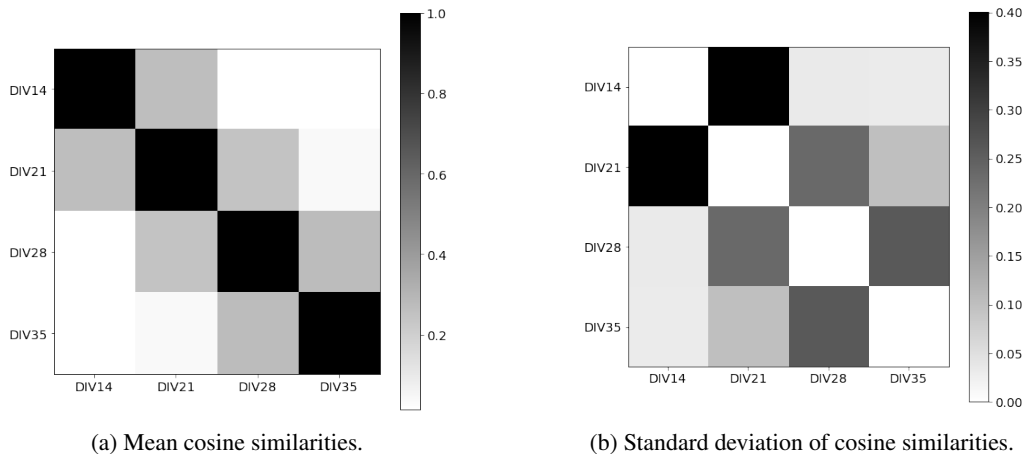


Figure 11: Mean and standard deviation of the cosine similarities between the vectors  $(h_t^{(1)}, \dots, h_t^{(K)})$  for each time period (DIV14, 21, 28 and 35) across the concatenated recordings.

Next, we look at the recovered structure for three cultures in more detail. We selected these recordings because they are representative of key types of behavior shown in Figure 10. The developmental trajectory of these cultures can be identified in Figure 10 by the color of the stars: P1B2 (pink), P5A2 (orange), and P3B1 (purple).

In the first culture, P1B2 (Figure 12), we see an initial increase in the number of subnetworks from DIV 14-28, followed by a mild consolidation of the network structure into new activity patterns at DIV 35. This illustrates the ability of the model to detect biologically relevant changes in subnetworks as the neuronal networks mature. The model detects seven different features (Figure 12b–12c), and the latent subgraphs reveal different combinations of electrodes detecting activity in these subnetworks (Figure 12d). From DIV 14 to DIV 28, we observe an increasing number of different features that are turned on (from 1 to 3). In addition, we see one feature introduced at DIV 21 remains active during DIV 28. However at DIV 35, one completely different feature is activated. These findings are consistent with an increase in network activity (Figure 12e) and density, illustrated in [28], at DIV14-28 and an increase in the mean nodal participation coefficient between DIV 28-35. When considering the spatial arrangement of the subnetworks (Figure 12d), we also observe a shift in participating nodes. During the first three weeks, the active nodes are more likely to be located in the middle or right side of the MEA, while in DIV35, the activity has shifted to the left. This may indicate that some subnetworks may increase or decrease in dominance in the overall network activity as the cultures mature.

The second culture, P5A2 (Figure 13), clearly demonstrates an increase in network complexity from DIV 14-35 (Figure 13b–13c), without the consolidation behavior seen in P1B2 at DIV 35. With no active features observed at DIV14, subnetwork 0 (Figure 13d) mainly comes from the baseline noise. As the neuronal networks mature, more features are activated, forming more complex subnetworks (Figure 13c–13d). We hypothesize that P5A2 may be following a similar developmental trajectory to P1A3, but with a slower start (as evidenced by the lack of correlated activity at DIV 14). As with P1A3, we observe the overall network structure becoming more complex as additional subnetworks are activated.

The third example, P3B1 (Figure 14), shows a growth and then stabilization of network complexity. At DIV 14, no active features are observed and most of the activity shown in subnetwork 0 is due to the low-level background process. From DIV 21-35, there is a developmental increase in the number of active features. We see high overlap in the active subnetworks: subnetwork  $\theta_1$  persists from DIV 14 – DIV 35, and subnetworks  $\theta_2$  and  $\theta_3$  persist from DIV 28 to DIV 35.

## Detect State Changes in Dynamic Networks

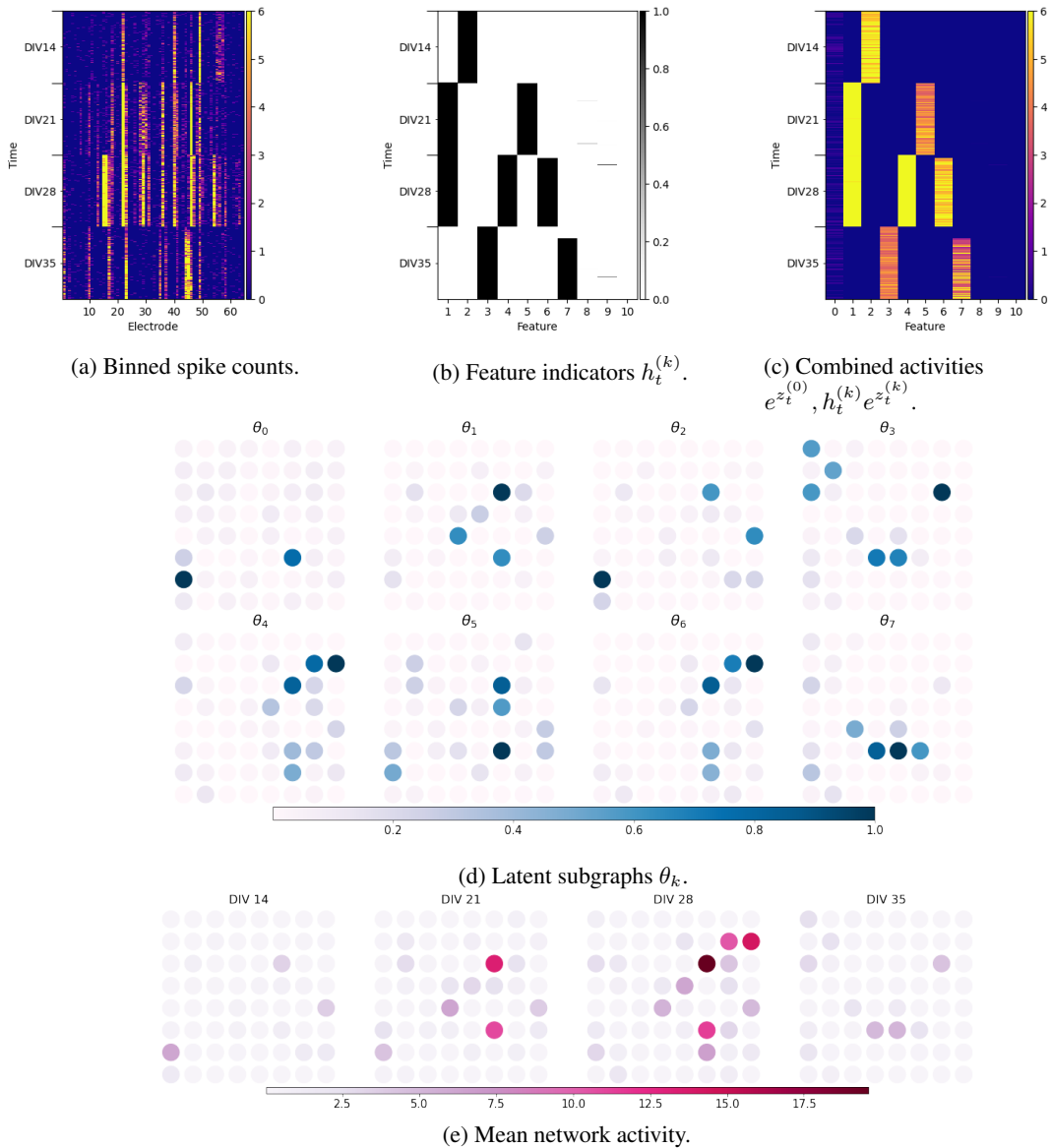


Figure 12: Development of human iPSC-derived NGN2 cortical neurons in culture P1B2. Figure 12a shows the raster plot from the concatenated spike train data from days-in-vitro (DIV) 14, 21, 28, and 35 with the spike count (binned in 1 second intervals) for the 64 electrodes (rows) over the four 10-minute recordings (x-axis unit is seconds). Figure 12b shows the latent features (rows) for the 10-minute MEA recordings from the four developmental time points (column). Color bar represents the probability of the feature being on (yellow) or off (purple). Figure 12c shows the combined activity (color bar) revealing the temporal dynamics within the on and off switching of the latent states within each MEA recording. Lighter colors (pink to yellow) show dominant features in contrast to features that are off (dark blue). Figure 12d shows heatmaps of the relative contribution (color) of individual electrodes (circles) to the subgraphs in the spatial arrangement of the MEA for subnetworks 0-7. Figure 12e shows heatmaps in the spatial arrangement of the MEA of the mean spike count (per second) per electrode (color) at the four developmental time points.

## Detect State Changes in Dynamic Networks

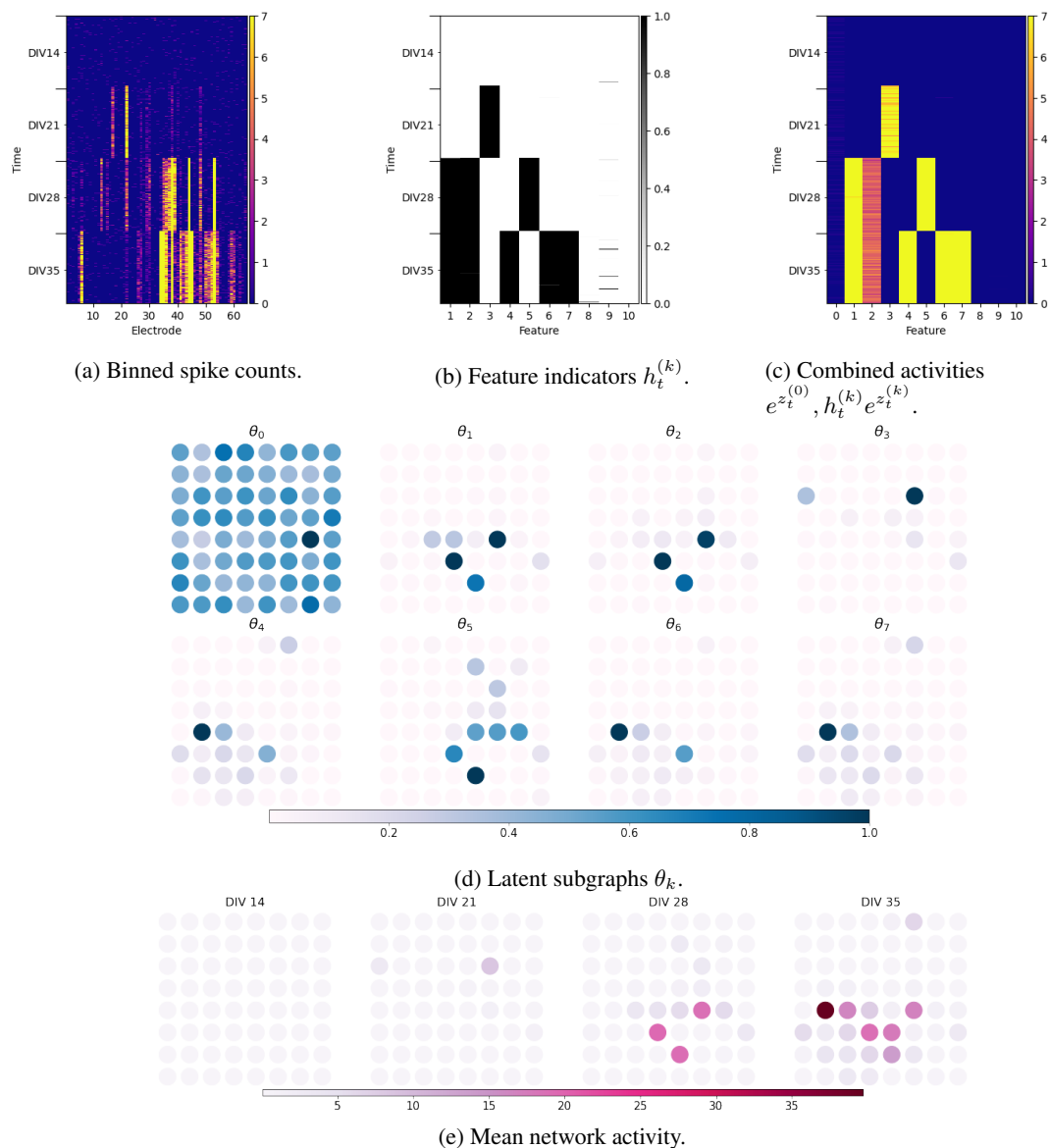


Figure 13: Development of human iPSC-derived NGN2 cortical neurons in culture P5A2. Figure 13a shows the raster plot from the concatenated spike train data from days-in-vitro (DIV) 14, 21, 28, and 35 with the spike count (binned in 1 second intervals) for the 64 electrodes (rows) over the four 10-minute recordings (x-axis unit is seconds). Figure 13b shows the latent features (rows) for the 10-minute MEA recordings from the four developmental time points (column). Color bar represents the probability of the feature being on (yellow) or off (purple). Figure 13c shows the combined activity (color bar) revealing the temporal dynamics within the on and off switching of the latent states within each MEA recording. Lighter colors (pink to yellow) show dominant features in contrast to features that are off (dark blue). Figure 13d shows heatmaps of the relative contribution (color) of individual electrodes (circles) to the subgraphs in the spatial arrangement of the MEA for subnetworks 0-5. Figure 13e shows heatmaps in the spatial arrangement of the MEA of the mean spike count (per second) per electrode (color) at the four developmental time points.



## Detect State Changes in Dynamic Networks

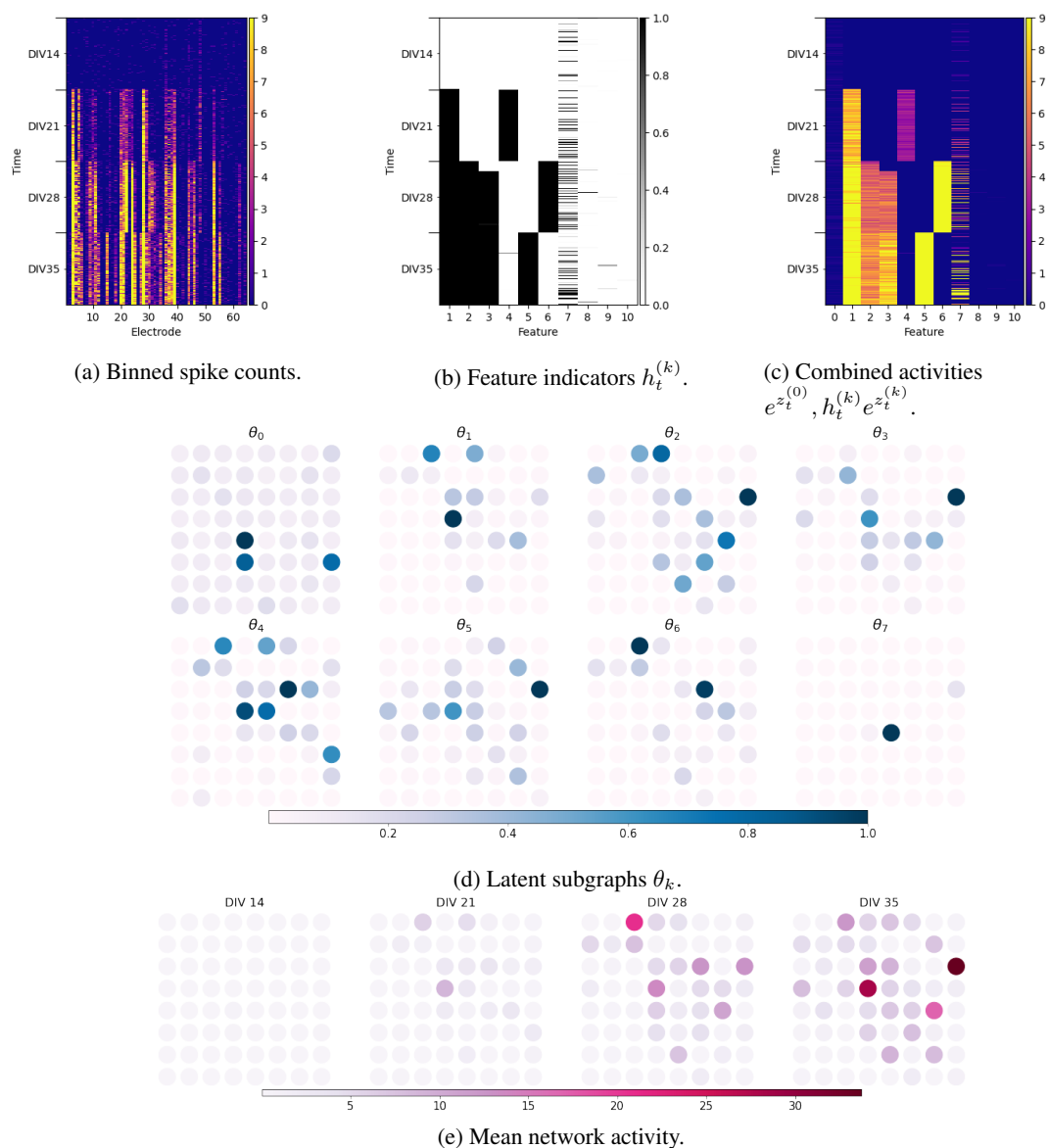


Figure 14: Development of human iPSC-derived NGN2 cortical neurons in culture P3B1. Figure 14a shows the raster plot from the concatenated spike train data from days-in-vitro (DIV) 14, 21, 28, and 35 with the spike count (binned in 1 second intervals) for the 64 electrodes (rows) over the four 10-minute recordings (x-axis unit is seconds). Figure 13b shows the latent features (rows) for the 10-minute MEA recordings from the four developmental time points (column). Color bar represents the probability of the feature being on (yellow) or off (purple). Figure 13c shows the combined activity (color bar) revealing the temporal dynamics within the on and off switching of the latent states within each MEA recording. Lighter colors (pink to yellow) show dominant features in contrast to features that are off (dark blue). Figure 13d shows heatmaps of the relative contribution (color) of individual electrodes (circles) to the subgraphs in the spatial arrangement of the MEA for subnetworks 0-7. Figure 13e shows heatmaps in the spatial arrangement of the MEA of the mean spike count (per second) per electrode (color) at the four developmental time points.

### **Conclusion**

The model performs well on MEA data from murine primary hippocampal cultures and from human iPSC-derived cortical cultures. It captures a developmental increase in the number of subnetworks and the likelihood of these subnetworks being on during the MEA recordings. This model provides an important tool for neurobiologists studying brain development and brain disorders with MEA recordings. It extends the tools beyond pair-wise comparisons to detect functional connectivity and identifies patterns of activity from subnetworks of different sizes that can vary on the scale of seconds to minutes during the MEA recording. This will enable neurobiologists to investigate differences in network complexity, capacity for information sharing, and stability versus flexibility of state switching in subnetworks. As the method uses spike train data, it may also be useful for analysis of data from other multielectrode recordings (e.g., Neuropixel probes), which may be performed *in vivo*, although significantly more than 64 electrodes would likely increase the computational demands. This method could also be used with MEA recordings to compare the effect of drugs on modulating network states *in vitro* or the effect of genetic mutations on the number of states and frequency of state switching. Thus, this approach may inform future mechanistic and therapeutic investigations in human-derived or murine models of neurological disorders.

### References

- [1] Guy Ackerson and K Fu. On state estimation in switching environments. *IEEE Transactions on Automatic Control*, 15(1):10–17, 1970. [3](#)
- [2] Philip Becker-Ehmck, Jan Peters, and Patrick Van Der Smagt. Switching linear dynamics for variational Bayes filtering. In *International Conference on Machine Learning*, pages 553–562. PMLR, 2019. [5](#)
- [3] Anne-Claude Camproux, Francois Saunier, Guy Chouvet, Jean-Christophe Thalabard, and Guy Thomas. A hidden Markov model approach to neuron firing patterns. *Biophysical Journal*, 71(5):2404–2412, 1996. [3](#)
- [4] Zhe Dong, Bryan Seybold, Kevin Murphy, and Hung Bui. Collapsed amortized variational inference for switching nonlinear dynamical systems. In *International Conference on Machine Learning*, pages 2638–2647. PMLR, 2020. [3](#)
- [5] Julia H Downes, Mark W Hammond, Dimitris Xydias, Matthew C Spencer, Victor M Becerra, Kevin Warwick, Ben J Whalley, and Slawomir J Nasuto. Emergence of a small-world functional network in cultured neurons. *PLoS computational biology*, 8(5):e1002522, 2012. [2](#)
- [6] Victor Geadah, International Brain Library, and Jonathan W Pillow. Parsing neural dynamics with infinite recurrent switching linear dynamical systems. In *International Conference on Learning Representations*, 2024. [2](#)
- [7] Zoubin Ghahramani. An introduction to hidden Markov models and Bayesian networks. *International Journal of Pattern Recognition and Artificial Intelligence*, 15(01):9–42, 2001. [3](#)
- [8] Zoubin Ghahramani and Michael Jordan. Factorial hidden Markov models. *Advances in Neural Information Processing Systems*, 8, 1995. [2](#), [4](#)
- [9] Simon J Godsill, Arnaud Doucet, and Mike West. Monte Carlo smoothing for nonlinear time series. *Journal of the American Statistical Association*, 99(465):156–168, 2004. [3](#)
- [10] Mark D Humphries. Dynamical networks: Finding, measuring, and tracking neural population activity using network science. *Network Neuroscience*, 1(4):324–338, 2017. [2](#)
- [11] Eric Jang, Shixiang Gu, and Ben Poole. Categorical reparameterization with Gumbel-softmax. In *International Conference on Learning Representations*, 2017. [3](#)
- [12] Diederik P. Kingma and Max Welling. Auto-encoding variational Bayes. In *International Conference on Learning Representations*, 2014. [2](#), [3](#), [6](#)
- [13] Dieterich Lawson, Allan Raventós, Andrew Warrington, and Scott Linderman. Sixo: Smoothing inference with twisted objectives. In *Advances in Neural Information Processing Systems*, volume 35, pages 38844–38858, 2022. [3](#)
- [14] Tuan Anh Le, Maximilian Igl, Tom Rainforth, Tom Jin, and Frank Wood. Auto-encoding sequential Monte Carlo. In *International Conference on Learning Representations*, 2018. [3](#)
- [15] Jie Li, Xiuli Chen, and Zheng Li. Spike detection and spike sorting with a hidden Markov model improves offline decoding of motor cortical recordings. *Journal of Neural Engineering*, 16(1):016014, 2018. [3](#)
- [16] S. Linderman, M. Johnson, A. Miller, Adams R., D. Blei, and L. Paninski. Bayesian learning and inference in recurrent switching linear dynamical systems. In *Artificial Intelligence and Statistics*, pages 914–922, 2017. [2](#), [3](#), [8](#)
- [17] Chris J Maddison, John Lawson, George Tucker, Nicolas Heess, Mohammad Norouzi, Andriy Mnih, Arnaud Doucet, and Yee Teh. Filtering variational objectives. *Advances in Neural Information Processing Systems*, 30, 2017. [3](#)
- [18] Chris J. Maddison, Andriy Mnih, and Yee Whye Teh. The concrete distribution: A continuous relaxation of discrete random variables. In *International Conference on Learning Representations*, 2017. [2](#), [3](#)

## Detect State Changes in Dynamic Networks

- [19] Christian Naesseth, Scott Linderman, Rajesh Ranganath, and David Blei. Variational sequential Monte Carlo. In *Artificial Intelligence and Statistics*, pages 968–977. PMLR, 2018. [3](#)
- [20] Josue Nassar, Scott W Linderman, Monica Bugallo, and Il Memming Park. Tree-structured recurrent switching linear dynamical systems for multi-scale modeling. In *International Conference on Learning Representations*, 2019. [2](#), [3](#)
- [21] César Ojeda, Bogdan Georgiev, Kostadin Cvejovski, Jannis Schucker, Christian Bauckhage, and Ramsés J Sánchez. Switching dynamical systems with deep neural networks. In *International Conference on Pattern Recognition*, pages 6305–6312. IEEE, 2021. [3](#)
- [22] Jimmy Olsson and Tobias Ryden. Rao-Blackwellization of particle Markov chain Monte Carlo methods using forward filtering backward sampling. *IEEE Transactions on Signal Processing*, 59(10):4606–4619, 2011. [3](#)
- [23] John Paisley, David M Blei, and Michael I Jordan. Variational Bayesian inference with stochastic search. In *International Conference on Machine Learning*, pages 1363–1370, 2012. [3](#)
- [24] Liam Paninski, Yashar Ahmadian, Daniel Gil Ferreira, Shinsuke Koyama, Kamiar Rahnama Rad, Michael Vidne, Joshua Vogelstein, and Wei Wu. A new look at state-space models for neural data. *Journal of Computational Neuroscience*, 29:107–126, 2010. [2](#)
- [25] Biljana Petreska, Byron M Yu, John P Cunningham, Gopal Santhanam, Stephen Ryu, Krishna V Shenoy, and Maneesh Sahani. Dynamical segmentation of single trials from population neural data. *Advances in Neural Information Processing Systems*, 24, 2011. [2](#), [3](#)
- [26] Manuel S Schroeter, Paul Charlesworth, Manfred G Kitzbichler, Ole Paulsen, and Edward T Bullmore. Emergence of rich-club topology and coordinated dynamics in development of hippocampal functional networks in vitro. *Journal of Neuroscience*, 35(14):5459–5470, 2015. [2](#), [9](#)
- [27] Manuel Schröter, Ole Paulsen, and Edward T Bullmore. Micro-connectomics: probing the organization of neuronal networks at the cellular scale. *Nature Reviews Neuroscience*, 18(3):131–146, 2017. [1](#), [2](#)
- [28] Timothy PH Sit, Rachael C Feord, Alexander WE Dunn, Jeremi Chabros, David Oluigbo, Hugo H Smith, Lance Burn, Elise Chang, Alessio Boschi, Yin Yuan, George M Gibbons, Mahsa Khayat-Khoei, Francesco De Angelis, Erik Hemberg, Martin Hemberg, Madeline A Lancaster, Andras Lakatos, Stephen J Eglén, Ole Paulsen, and Susanna B Mierau. MEA-NAP compares microscale functional connectivity, topology, and network dynamics in organoid or monolayer neuronal cultures. *bioRxiv*, 2024. [2](#), [8](#), [9](#), [13](#), [14](#)
- [29] Jimmy Smith, Scott Linderman, and David Sussillo. Reverse engineering recurrent neural networks with Jacobian switching linear dynamical systems. *Advances in Neural Information Processing Systems*, 34:16700–16713, 2021. [3](#)
- [30] Theophane Weber, Nicolas Heess, Ali Eslami, John Schulman, David Wingate, and David Silver. Reinforced variational inference. In *Advances in Neural Information Processing Systems Workshops*, 2015. [3](#)
- [31] Mike West. Bayesian dynamic modelling. *Bayesian Inference and Markov Chain Monte Carlo: In Honour of Adrian FM Smith*, 145:166, 2013. [3](#)
- [32] Dimitris Xydas, Julia H Downes, Matthew C Spencer, Mark W Hammond, Slawomir J Nasuto, Benjamin J Whalley, Victor M Becerra, and Kevin Warwick. Revealing ensemble state transition patterns in multi-electrode neuronal recordings using hidden Markov models. *IEEE Transactions on Neural Systems and Rehabilitation Engineering*, 19(4):345–355, 2011. [3](#)